

<https://doi.org/10.1038/s41535-024-00654-2>

# Lattice-commensurate skyrmion texture in a centrosymmetric breathing kagome magnet

Check for updates

Max Hirschberger<sup>1,2</sup>✉, Bertalan G. Szigeti<sup>3</sup>, Mamoun Hemmida<sup>3</sup>, Moritz M. Hirschmann<sup>2</sup>, Sebastian Esser<sup>1</sup>, Hiroyuki Ohsumi<sup>4</sup>, Yoshikazu Tanaka<sup>4</sup>, Leonie Spitz<sup>2,11</sup>, Shang Gao<sup>2,12</sup>, Kamil K. Kolincio<sup>2,5</sup>, Hajime Sagayama<sup>6</sup>, Hironori Nakao<sup>6</sup>, Yuichi Yamasaki<sup>7</sup>, László Forró<sup>8</sup>, Hans-Albrecht Krug von Nidda<sup>3</sup>, Istvan Kezsmarki<sup>3</sup>, Taka-hisa Arima<sup>2,9</sup> & Yoshinori Tokura<sup>1,2,10</sup>

Skyrmion lattices (SkL) in centrosymmetric materials typically have a magnetic period on the nanometer-scale, so that the coupling between magnetic superstructures and the underlying crystal lattice cannot be neglected. We reveal the commensurate locking of a SkL to the atomic lattice in  $\text{Gd}_3\text{Ru}_4\text{Al}_{12}$  via high-resolution resonant elastic x-ray scattering (REXS). Weak easy-plane magnetic anisotropy, demonstrated here by a combination of ferromagnetic resonance and REXS, penalizes placing a skyrmion core on a site of the atomic lattice. Under these conditions, a commensurate SkL, locked to the crystal lattice, is stable at finite temperatures – but gives way to a competing incommensurate ground state upon cooling. We discuss the role of Umklapp-terms in the Hamiltonian for the formation of this lattice-locked state, its magnetic space group, and the role of slight discommensurations, or (line) defects in the magnetic texture. We also contrast our findings with the case of SkLs in noncentrosymmetric material platforms.

Magnetic skyrmion lattices (SkLs) are periodic arrays of vortex-like spin structures. In SkLs, magnetic moments are twisted into a knot, covering all directions of a sphere as we traverse a single magnetic unit cell (UC) (Fig. 1a)<sup>1–3</sup>. These vortices were first described as topological solitons using the concepts of field theory, and such continuum models are most suitable when the magnetic UC is at least two orders of magnitude larger than the underlying crystallographic UC<sup>3–5</sup>. With a focus on frustrated, i.e. competing, interactions, recent theoretical work<sup>6–10</sup> has proposed SkL formation in a high-symmetry context without spin-orbit driven Dzyaloshinskii-Moriya interactions, paving the way for the experimental observation of SkL phases with magnetic period on the nanometer-scale in centrosymmetric insulators and metals<sup>3,11–14</sup>. These quasi-discrete SkLs have raised hopes of enhanced functional responses, especially those related to the interplay of

emergent electromagnetic fields with conduction electron (Bloch) waves, or with incident light waves<sup>3,15–20</sup>.

Evidence for coupling between the atomic lattice and skyrmion textures with lattice spacing 2 – 3 nanometers has emerged in tetragonal magnets: Centrosymmetric alloys host square and rhombic skyrmion lattices<sup>3,21</sup>, and non-centrosymmetric  $\text{EuNiGe}_3$  exhibits a fascinating helicity reversal upon entering the SkL phase, where the magnetic texture breaks the sense of rotation prescribed by its polar structure<sup>13,14</sup>. A key open challenge is the demonstration of a commensurate locking (C-locking) transition of the SkL's spin superstructure to the underlying lattice potential in such a centrosymmetric bulk material. This phenomenon is conceptually related to instabilities of the skyrmion vortex core anticipated for spin-1 systems<sup>22</sup> and its observation would provide a bridge between – usually – large-scale SkL

<sup>1</sup>Department of Applied Physics and Quantum-Phase Electronics Center, The University of Tokyo, Bunkyo-ku, Tokyo 113-8656, Japan. <sup>2</sup>RIKEN Center for Emergent Matter Science (CEMS), Wako, Saitama 351-0198, Japan. <sup>3</sup>Experimental Physics V, Center for Electronic Correlations and Magnetism, University of Augsburg, 86135 Augsburg, Germany. <sup>4</sup>RIKEN SPring-8 Center, 1-1-1 Kouto, Sayo, Hyogo 679-5148, Japan. <sup>5</sup>Faculty of Applied Physics and Mathematics, Gdańsk University of Technology, Narutowicza 11/12, 80-233 Gdańsk, Poland. <sup>6</sup>Institute of Materials Structure Science, High Energy Accelerator Research Organization, Tsukuba, Ibaraki 305-0801, Japan. <sup>7</sup>Research and Services Division of Materials Data and Integrated System (MaDIS), National Institute for Materials Science (NIMS), Tsukuba 305-0047, Japan. <sup>8</sup>Stavropoulos Center for Complex Quantum Matter, Department of Physics and Astronomy, University of Notre Dame, Notre Dame, IN 46556, USA. <sup>9</sup>Department of Advanced Materials Science, The University of Tokyo, Kashiwa 277-8561, Japan. <sup>10</sup>Tokyo College, The University of Tokyo, Bunkyo-ku, Tokyo 113-8656, Japan. <sup>11</sup>Present address: Paul Scherrer Institut, Forschungsstrasse 111, 5232 Villigen PSI, Switzerland, <sup>12</sup>Present address: Department of Physics, University of Science and Technology of China, Hefei 230026, China. ✉e-mail: [hirschberger@ap.t.u-tokyo.ac.jp](mailto:hirschberger@ap.t.u-tokyo.ac.jp)

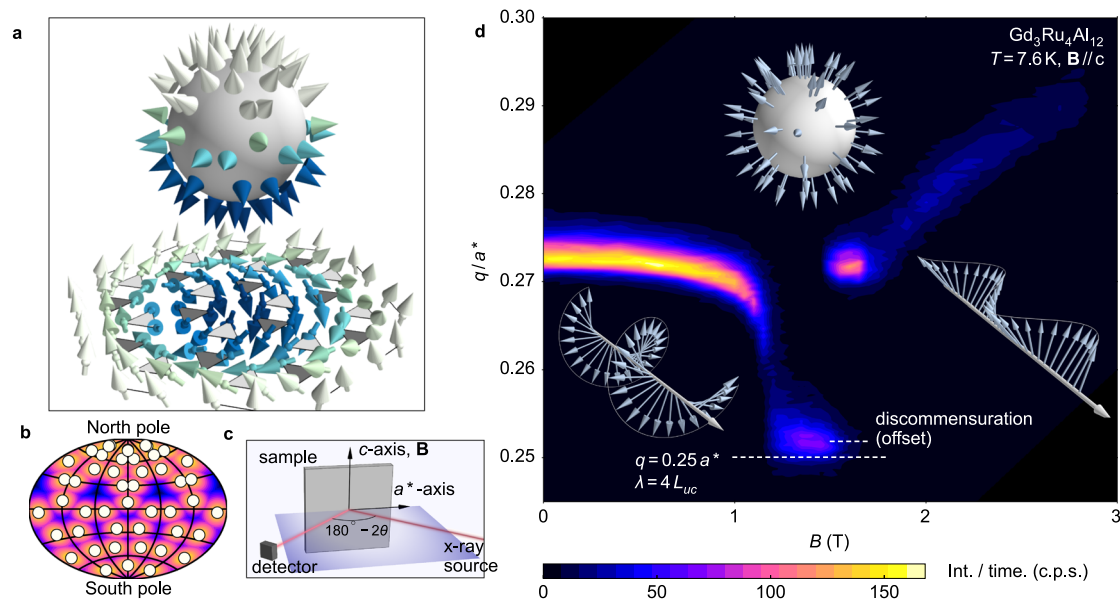


**Fig. 1 | Commensurate locking of the skyrmion lattice phase in  $Gd_3Ru_4Al_{12}$  (GRA).** **a** Magnetic moments of a skyrmion winding a sphere (top), and corresponding two-dimensional magnetic moment texture in real space (bottom). Each arrow corresponds to a site of the magnetic sublattice (Supplementary Note 1). **b** Map projection showing a hemisphere of (a) unfolded, with white dots indicating directions of magnetic moments. The colour code indicates the distance of each point on the sphere from the nearest moment on the sphere, in radians. **c** Experimental geometry of resonant elastic x-ray scattering (REXS) at the Gd- $L_2$  absorption edge, where the pink line is the trajectory of the x-ray beam. **d** Scattering

intensity in REXS as a function of magnetic field ( $B$ ) and momentum transfer  $q$  from  $\mathbf{q} = (q, 0, 0)$ ;  $q = 0.25$  corresponds to  $\lambda = 2\pi/q = 4 L_{uc}$ , four times the projection of the lattice constant parallel to  $\mathbf{q}$  (Supplementary Fig. 1). Incommensurate proper screw (IC-PS), commensurate skyrmion lattice (C-SkL), and IC fan phases are illustrated by insets. In C-SkL, the periodicity of the magnetic texture is locked to the crystal lattice up to a weak discommensuration (offset) of  $\Delta q = 0.0018$  r.l.u.  $B$  denotes magnetic induction after demagnetization correction (Supplementary Fig. 4). Supplementary Fig. 6 and Supplementary Fig. 7 show raw data used to create this colormap and the results of Gaussian fitting to the data, respectively.

spin textures in materials with broken inversion symmetry, and canted antiferromagnetism on the scale of a single unit cell. Indeed, theory predicts such C-locking based on Ruderman-Kittel-Kasuya-Yosida (RKKY) interactions and magnetic anisotropy, when the length scale of magnetic textures approaches the size of a crystallographic UC<sup>23</sup>. Among inversion breaking material platforms, the hcp-Fe/Ir(111) interface has been reported to exhibit C-locking using imaging techniques, although fcc-Fe/Ir(111) forms a lattice-incommensurate structure<sup>6,24–26</sup>. However, such locking between the periodicity of a magnetic skyrmion lattice and the underlying crystal structure has never been observed in a bulk material.

Using precise resonant x-ray measurements, we report a commensurate skyrmion lattice (C-SkL) surrounded by incommensurate (IC) phases in bulk samples of the centrosymmetric intermetallic  $Gd_3Ru_4Al_{12}$ , locked to the distorted kagome network of magnetic gadolinium ions. We discuss this state based on (weak) single-ion anisotropy  $K_1$ , as supported by electron-spin resonance experiments.

For large classical spins, calculations on both triangular and breathing kagome lattices show that, if the single-ion anisotropy is of easy-plane type (easy-axis type), a commensurate skyrmion vortex may gain energy by locating its core at an interstitial site (on a lattice site)<sup>23,27</sup>; an incommensurate skyrmion lattice does not benefit from this type of energy gain (Supplementary Fig. 5). We illustrate this point in the lower part of Fig. 1a, depicting a realistic magnetic structure model for the C-SkL of  $Gd_3Ru_4Al_{12}$ , described by normalized vectors  $\mathbf{n}(x, y)$ , which is mapped onto a sphere using a stereographic projection, see Methods. Here, magnetic moments are conspicuously absent at the poles (Fig. 1a, upper). The sparsity of magnetic moments at the poles becomes more apparent when unfolding the sphere using a cartographic projection (Fig. 1b and Supplementary Note 1).

## Results

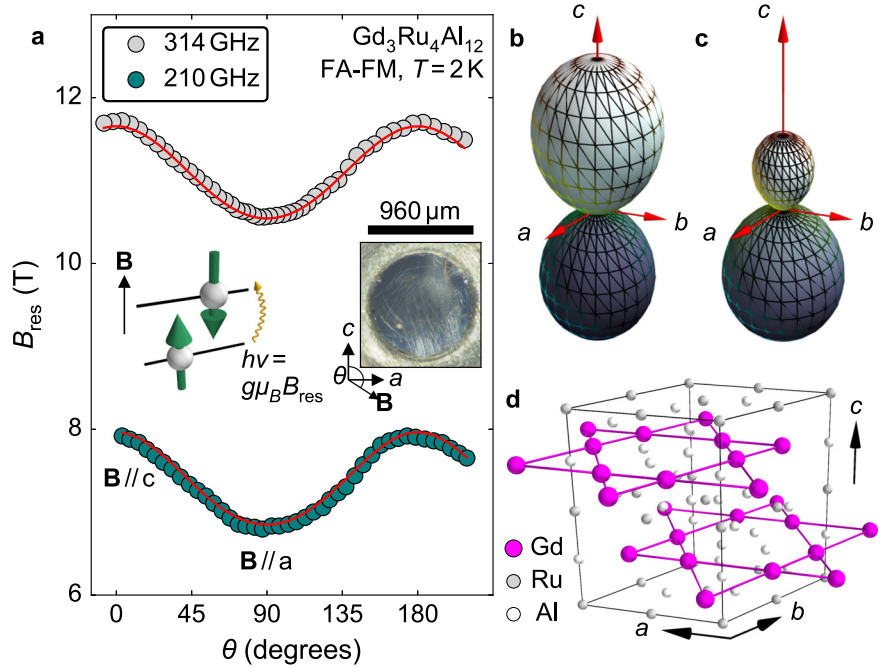
### Observation of a commensurate skyrmion lattice (C-SkL)

We use elastic x-ray scattering in resonance with the  $L_{2,3}$  absorption edge of gadolinium, setting the sample in reflection geometry to

precisely detect the magnetic period of each magnetic phase (Fig. 1c and Methods). Reporting data from a synchrotron light source, Fig. 1d depicts the core observation of this work: At moderate temperatures  $T = 7 - 8$  K, a magnetic field  $\mathbf{B}$  applied along the  $c$ -axis drives the incommensurate proper screw ground state (IC-PS) into a commensurate skyrmion lattice phase (C-SkL), and again to incommensurate fan-like order (IC-Fan). The C-locking of the SkL was not observed in a previous study<sup>11</sup>. The present and previous results are compared and summarized in Supplementary Fig. 4. Let  $a^*$  and  $c^*$  be the reciprocal space lattice constants for our target material  $Gd_3Ru_4Al_{12}$  in the hexagonal  $P6_3/mmc$  space group, where magnetic gadolinium ions form a kagome (star of David) lattice with a breathing distortion, corresponding to alternating bond distances. In zero magnetic field, the magnetic modulation wavevector is  $\mathbf{q} = (q, 0, 0)$  with  $q \approx 0.272 a^*$  or wavelength  $\lambda \approx 3.7 L_{uc}$ , where  $L_{uc}$  is the dimension of the crystallographic UC projected parallel to  $\mathbf{q}$  (Supplementary Fig. 1). The wavevector's length  $q$  decreases with  $B$  in IC-PS, approaching a discontinuous jump at the first-order transition<sup>11</sup> towards  $q = 0.25 a^*$  in C-SkL. The magnetic period  $\lambda$  in C-SkL is very close to  $4 L_{uc}$ , with a slight offset indicated by two dashed horizontal lines in Fig. 1d. The role of this slight offset, or discommensuration  $\lambda_{disc}$ , is discussed below. To further support the C-locking at  $q = 0.25 a^*$ , we demonstrate in Supplementary Fig. 7 that the peak profiles are within less than one standard deviation from the commensurate value, and in Supplementary Fig. 10 that  $q$  has weak temperature dependence in C-SkL as compared to IC-PS.

In the regime labeled as C-SkL in Fig. 1, previous real-space imaging experiments have observed vortex structures<sup>11</sup>, and precise Hall effect measurements demonstrate that the noncoplanar magnetic state that is easily destroyed by a slight in-plane magnetic field<sup>28</sup>. However, neither this prior work nor the present REXS technique are able to determine whether the skyrmion core is located on a crystallographic lattice site, or on an interstitial site. This question of the relative phase shift between magnetic

**Fig. 2 | Magnetic anisotropy in field-polarized ferromagnetic (FA-FM), incommensurate proper screw (IC-PS), and skyrmion lattice (C-SkL) phases of  $Gd_3Ru_4Al_{12}$ .** **a** Resonance field  $B_{res} = \mu_0 H_{res}$  in ferromagnetic resonance (FMR) experiments in FA-FM at 210 and 314 GHz (grey and green markers). Red lines: Fit to the data according to Smit-Beliers-Suhl, corresponding to weak in-plane anisotropy, see Methods. Left inset: principle of FMR, where transitions between up and down moments are induced by microwave radiation in a cavity. Right inset: geometry of magnetic field  $\mathbf{B}$  with respect to the principal axes of a disk-shaped single crystal. **b, c** Anisotropic energy landscape  $F_{anis} = K_1 \cos^2(\theta) - E_Z \cos(\theta)$  in zero field (Zeeman term  $E_Z = 0$ ) and finite magnetic field ( $E_Z/K_1 = 0.3$ ), as a function of the direction of the bulk magnetization vector  $\mathbf{M}$ . **d** Crystal structure of  $Gd_3Ru_4Al_{12}$  with magnetic breathing kagome sublattice of gadolinium, shown in magenta.



texture and crystal lattice can be addressed by measurements of single-ion anisotropy, combined with theoretical modeling: We turn to the ferromagnetic resonance (FMR) technique in the following section.

### Single-ion anisotropy in $Gd_3Ru_4Al_{12}$

We prepared a cylindrical disk-shaped sample for ferromagnetic resonance (FMR) experiments, spanned by the crystallographic  $a$  and  $c$  directions (Fig. 2a, right inset). This highly symmetric geometry allows for simple data analysis when rotating the magnetic field in the plane of the disk, see Methods. In the experiment, we drive the crystal into the field-aligned ferromagnetic (FA-FM) state with a large magnetic field, irradiate it with microwaves of frequency  $\nu = 210$  or  $314$  GHz, and observe a change of its reflectivity when the microwaves excite a resonance between moment-up and -down states (Fig. 2a, left inset).

In Fig. 2a, the anisotropic part of the free energy  $F_{anis} = K_1 \cos^2(\theta)$  is deduced in FA-FM from a fit to the angular dependence of the FMR resonance field  $B_{res}$ ; we disregard anisotropy constants beyond the first order, see Methods. Using the saturation magnetization  $M_S = 7 \mu_B / Gd^{3+}$ , our fit yields easy-plane anisotropy with  $K_1 = -0.13$  meV /  $Gd^{3+}$ . Therefore, the anisotropy field  $B_{ani}$  can be calculated as  $\mu_0 |2K_1| / M_S = 0.74$  Tesla. As compared to magnetization measurements in Supplementary Fig. 11, the present FMR study yields enhanced precision; field-dependent FMR experiments separate  $g$ -factor anisotropy and exchange anisotropy from the single-ion term, see Methods. Figure 2b, c illustrates the resulting iso-energy surfaces  $F_{anis}(\theta, \varphi)$  in zero (finite) magnetic field along the  $c$ -axis, respectively, where the spherical coordinates refer to the direction of the sample's bulk magnetization  $\mathbf{M}$ .

### Anisotropy and anharmonic distortion of proper screw and skyrmion phases

Easy-plane anisotropy ( $K_1 < 0$ ) can also be verified semi-quantitatively by resonant elastic x-ray scattering in the ordered phases with periodic long-range order. Figure 1c shows the geometry of our experiment with polarization analysis: the purple scattering plane is spanned by the wavevectors  $\mathbf{k}_i$  and  $\mathbf{k}_f$  of the incoming and outgoing x-ray beams, with beam polarization  $\varepsilon_i$  and  $\varepsilon_f$ , respectively. We choose the incoming beam polarization  $\varepsilon_i$  to lie within the scattering plane for all our experiments ( $\pi$ -polarization). While the data in Fig. 1d represents a sum of scattered

photons with all possible  $\varepsilon_f$ , we now add an analyser plate before the x-ray detector to separate two components of the scattered beam:  $I_{\pi-\pi'}$  and  $I_{\pi-\sigma'}$  with  $\varepsilon_f$  within or perpendicular to the scattering plane, respectively. From the scattered intensities at various magnetic reflections, we extract the ratio, see Methods,

$$R \sin^2(2\theta) = I_{\pi-\sigma'} \sin^2(2\theta) / I_{\pi-\pi'} = [\mathbf{k}_i \cdot \mathbf{m}_{ab}(\mathbf{q}) / m_c(\mathbf{q})]^2 \quad (1)$$

with  $\mathbf{m}_{ab}$  the component of the modulated magnetic moment in the scattering plane. The expected behavior of IC-PS (spin plane  $a$ - $c$ ) and IC cycloid (spin plane  $a^*$ - $c$ ) is indicated in Fig. 3b by black and green dashed lines, respectively; a line with positive slope indicates IC-PS character. Supplementary Fig. 3 shows representative raw data, as used to create this panel.

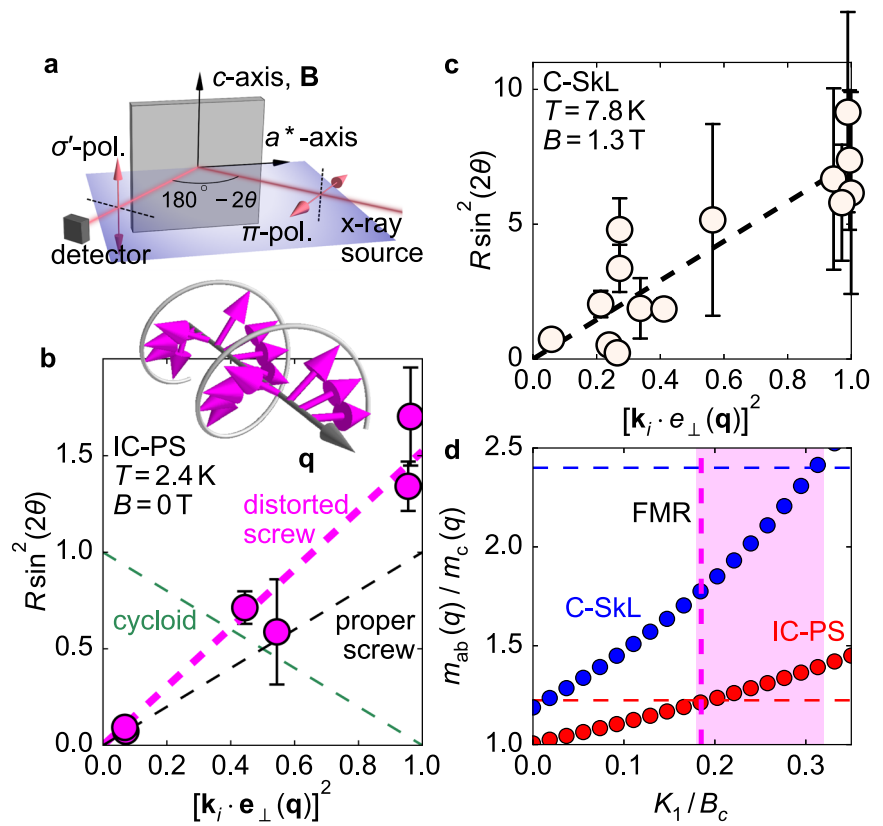
Beyond identifying the PS character of the spin modulation, this analysis allows us to estimate the effect of single-ion anisotropy in IC-PS. Specifically, we observe an elliptic distortion, i.e., a deviation from the proper screw model. Figure 3b, c displays maximum values of  $R \sin^2(2\theta)$  around 1.5 (IC-PS) and 7 (C-SkL), so that Eq. (1) delivers  $m_{ab}(\mathbf{q}) / m_c(\mathbf{q})$  around 1.2 (IC-PS) and 2.6 (C-SkL). Figure 3b, inset, illustrates the proposed anharmonic distortion in IC-PS, where magnetic moments prefer to tilt towards the basal plane to gain anisotropy energy. In Fig. 3d, a simulation of REXS anisotropy as a function of  $K_1$  for a spin model in both IC-PS and C-SkL (Supplementary Note 1) shows that the experimentally observed ellipticity is consistent with the results of FMR in Fig. 2. Given the robust observation of  $K_1 < 0$  via various experimental techniques, we conclude that a C-SkL in magnetic space group  $P6_32'2'$  and with skyrmion core between lattice sites is stable in  $Gd_3Ru_4Al_{12}$  (Supplementary Note 2).

### Competition of commensurate and incommensurate phases

Figure 4a shows a magnetic field scan of x-ray scattering intensity at the lowest accessible temperature,  $T = 1.5$  K; see Supplementary Fig. 4 for detailed phase diagrams and comparison to prior work. In contrast to Fig. 1d, the C-SkL phase is now absent, being replaced by an incommensurate transverse conical (IC-TC) state<sup>11</sup>.

We compare the experimental and theoretical results for  $Gd_3Ru_4Al_{12}$  to earlier studies of magnetism in elemental rare earth metals. Various scenarios for the interplay of commensurate (C) and IC phases have been advanced<sup>29,30</sup>: One typical observation in systems with strong single-ion

**Fig. 3 | Magnetic anisotropy in ordered states of Gd<sub>3</sub>Ru<sub>4</sub>Al<sub>12</sub>.** **a** Experimental geometry of resonant elastic x-ray scattering (REXS) with (in contrast to Fig. 1c) polarization analysis.  $\pi$  and  $\sigma$  indicate x-rays (photons) polarized parallel and perpendicular to the scattering plane (purple), respectively. **b** Elliptic distortion of IC-PS determined by polarization analysis in REXS.  $I_{\pi-\sigma}$ ,  $I_{\pi-\pi}$ ,  $\mathbf{k}_i$ , and  $\mathbf{e}_\perp$  are integrated intensities in the polarization-flipping and polarization-conserving scattering channels, the incoming beam's wavevector, and the in-plane direction perpendicular to the propagation vector  $\mathbf{q}$  of IC-PS, as in Eq. (1). Green, black, and magenta dashed lines indicate model predictions for spherical cycloid, spherical proper screw, and elliptically distorted screw, the latter being shown in the inset cartoon. The value of  $R\sin^2(2\theta)$  at the right boundary of the panel corresponds to the elliptic distortion  $(m_{ab}/m_c)^2$  as defined in Eq. (1). **c** Analogous data for the commensurate skyrmion (C-SkL) state; see Supplementary Table 1 for more details. Note the different  $y$ -axis range as compared to (b). **d** Spin-model calculation of elliptic distortion in IC-PS and C-SkL as a function of anisotropy constant  $K_1$ , normalized to the critical field  $B_c = 4$  T for transition to the field-aligned ferromagnetic (FA-FM) state. Dashed horizontal lines, dashed vertical line, and highlighted area indicate the experimental values for the ellipticity, the value of  $K_1$  from FMR, and the range of  $K_1$  consistent with REXS experiments, respectively. Error bars in (b, c) are obtained from Gaussian fits to line profiles as in Supplementary Fig. 3, with quadratic error propagation for the intensity ratio.



anisotropy is the appearance of spin-slip structures in the IC order, and eventual *squaring up* at low temperatures. In this scenario, thermal fluctuations at higher  $T$  locally reduce the ordered magnetic moment, allowing for the formation of IC magnetism close to the Néel point, e.g. in elemental Holmium<sup>29</sup>. Secondly, when single-ion anisotropy is much weaker than exchange interactions, C orders are favored at higher temperatures where short-range correlations dominate. However, they can give way to IC ground states as further-neighbor exchange gains importance upon cooling (e.g. ref. 31). Thirdly, in inversion breaking systems with strong Dzyaloshinskii-Moriya interactions, IC-C transitions appear at low temperature when solitonic distortions are introduced into an IC order via a magnetic field<sup>32–35</sup>, especially if a large charge gap is opened due to nesting<sup>35</sup>. The present study generalizes the second scenario to the case of complex, twisted magnetic textures, such as the C-SkL, with an important role for (weak) magnetic anisotropy.

We consider the observation of C-locking induced by magnetic fields, in our experiment, based on the single-ion contribution to the spin Hamiltonian (Supplementary Note 3)

$$\mathcal{H}_{\text{anis}} \propto -K_1 \sum_{\mathbf{G}} \sum_{\mathbf{q} \in \text{BZ}} S^z(\mathbf{q}) S^z(\mathbf{G} - \mathbf{q}) \left[ \sum_{\mathbf{d} \in \text{u.c.}} e^{i\mathbf{G} \cdot \mathbf{d}} \right] \quad (2)$$

where  $\mathbf{r} = \mathbf{R} + \mathbf{d}$  is the position of a magnetic ion, decomposed into a unit cell coordinate  $\mathbf{R}$  and an intra-cell coordinate;  $\mathbf{q}$  and  $\mathbf{G}$  are the momentum in the first Brillouin zone and a reciprocal lattice vector, respectively. Typically, a small number of Fourier modes  $\mathbf{q} = \mathbf{q}_v$  and  $\mathbf{G} = 0$  are selected in models of incommensurate helimagnetic ordering<sup>12,21,28</sup>. Meanwhile, C-locking is favored by the Umklapp terms  $\mathbf{G} \neq 0$ <sup>36,37</sup>, representing a coupling between the primary Fourier mode of a helimagnet and its higher harmonics. Specifically for the  $q = 0.25 a^*$  C-SkL in Gd<sub>3</sub>Ru<sub>4</sub>Al<sub>12</sub>,  $S(3\mathbf{q}) \cdot S(\mathbf{q})$  and  $S(2\mathbf{q})^2$  are the leading contributors, adding to  $\mathbf{G} = (1, 0, 0)$  and coupling the helimagnetic

order to the lattice. Application of a magnetic field to IC-PS enhances the elliptic distortion as demonstrated in Fig. 3, amplifies anharmonicity, shifts  $\mathbf{q}$  away from the value preferred by the exchange interaction and towards commensurability, and ultimately induces C-locking between the spin texture and the underlying lattice. In Supplementary Note 3, we thus derive an expression for the energetic contribution that depends on the position of the skyrmion core. Nevertheless, a full numerical treatment of Eq. (2) with large numbers of Fourier modes, to capture changes in the optimal  $\mathbf{q}$  – as well as changes in the cycloidal / screw character of the modulation – as a function of magnetic field and temperature, remains a challenge at present (Supplementary Note 1).

To explain the effect of single-ion anisotropy more intuitively, we initialize C-SkL and C-PS on the lattice and allow the magnetic moments to relax in the combined potential of exchange interaction, magnetic anisotropy, and external field (white/green arrows in Fig. 4b, c). The red arrows show a significant distortion of the textures, especially around the south pole. This density of strongly distorted moments is much larger for the C-PS state with quasi one-dimensional spin texture, which has an extended south pole region. In particular, the south pole direction of the magnetic moment sphere in Fig. 1a corresponds to a point (to a line) in case of a SkL (of a PS). We also calculated the  $z$ -projection of magnetic moments for a spin model of C-PS, C-SkL, and other orders, using our experimental  $K_1$  from FMR, thus confirming numerically the favorable pinning of the C-SkL due to stronger higher harmonics (Supplementary Fig. 5).

## Discussion

Figure 1d reveals a discommensuration of the magnetic lattice, i.e., a slight offset from  $q/a^* = 0.25$  that indicates occasional magnetic defects. The discommensuration effect is well understood in one-dimensional chain systems<sup>38</sup>: For example, the introduction of small amounts of chemical disorder causes proliferation of discommensurations in spin-Peierls chains,

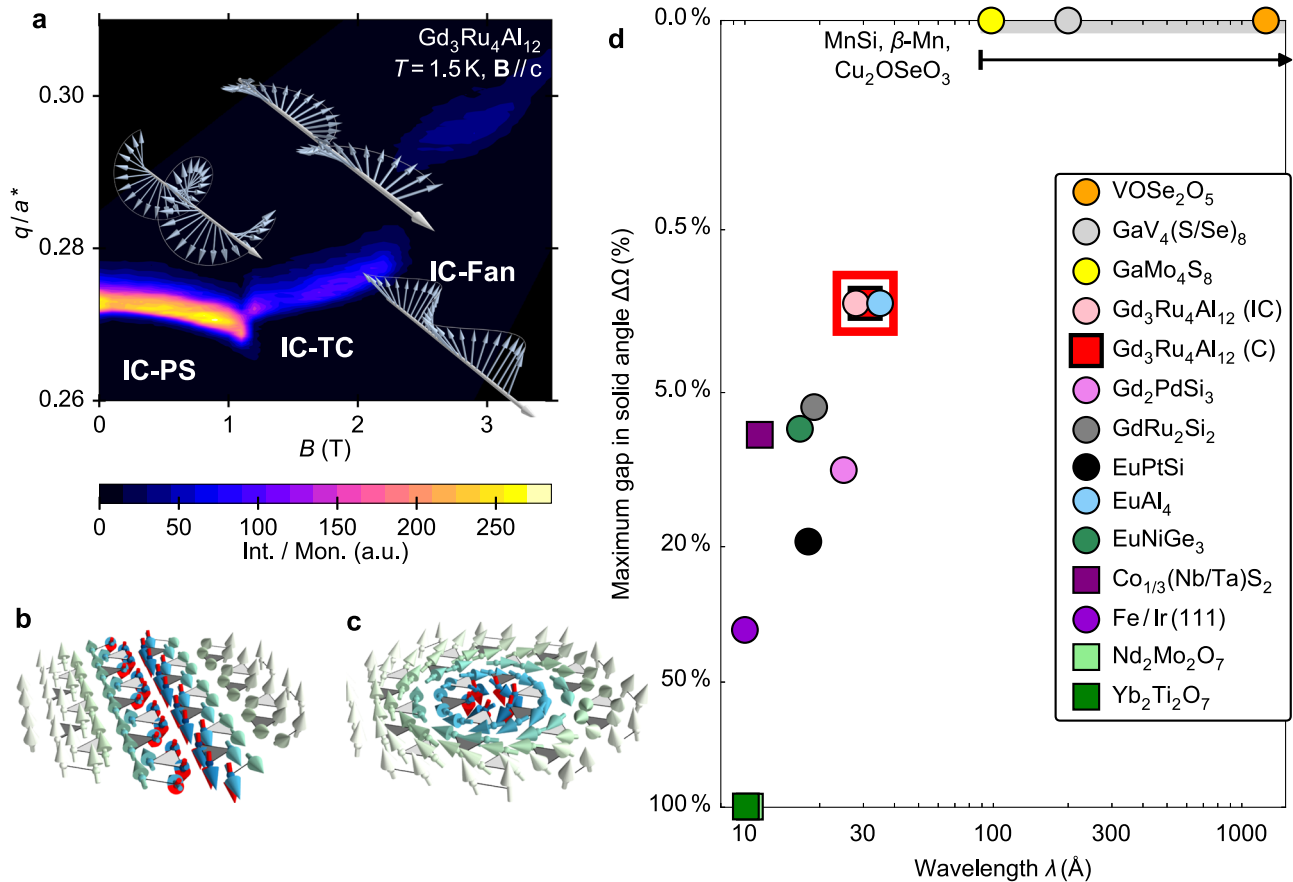


**Fig. 4 | Stability of the commensurate skyrmion lattice (C-SkL) as compared to other magnetic phases.** **a** Resonant x-ray scattering intensity, normalized to monitor counts, at base temperature ( $T = 1.5$  K). Three incommensurate (IC) magnetic phases are shown: from left to right, proper screw (IC-PS), transverse conical (IC-TC), and fan-like (IC-Fan) as illustrated by insets. Quantitative analysis of Gaussian line-scan profiles is given in Supplementary Fig. 8. **b, c** Distortion of proper screw (left) and skyrmion textures in anisotropy potential and external magnetic field along the  $z$ -direction (Supplementary Note 1). The undistorted

moment directions (red) are superimposed on those moments that have been rotated by more than a critical angle. **d** Relationship of magnetic texture dimensions ( $\lambda$ ) and coverage of directions on the sphere for various materials with noncoplanar textures and spin chirality<sup>3,11,13,14,44,45,51</sup>. At the center of the plot, the commensurate C-SkL state in  $Gd_3Ru_4Al_{12}$  is highlighted by a red box. On the  $y$ -axis, a continuous magnetic texture has zero *uncovered solid angle*, i.e. we assign a value of 0%. Note the stretched scale of the  $y$ -axis.

as manifested in a drop of  $\lambda_{disc}$  that ultimately destroys the commensurate (C) order<sup>39–42</sup>. Discommensurations in two dimensions, mostly line defects, also appear for surface-adsorbed atoms and in the multi-directional charge-density wave state of transition metal dichalcogenides such as  $2H-TaSe_2$ , where C-IC transitions have been extensively studied<sup>36,37</sup>. Among materials with two-dimensional spin textures, we compare to the C-SkL observed in an interfacial system<sup>24–26</sup>. For inversion-breaking hcp-Fe/Ir(111) (for centrosymmetric  $Gd_3Ru_4Al_{12}$ ), the spin structure is found to be commensurate within less than 10% (within 0.7%) of the magnetic period, and there is no (there is) evidence of C-IC transitions by cooling or application of a magnetic field. Based on measurements of magnetic anisotropy and modeling, we argue here that  $Gd_3Ru_4Al_{12}$  has skyrmion cores on interstitial lattice sites, as does hcp-Fe/Ir(111); further that the discommensuration represents the appearance of line defects (characteristic spacing  $\lambda_{disc} = 430$  nm) in the former – while phase-slip domain walls (spacing  $\sim 10$  nm) and domains of the net magnetization (spacing  $\sim 30$  nm) have been observed in the latter. We note that domain walls of the skyrmion helicity may appear in the bulk C-SkL of centrosymmetric materials<sup>6,43</sup>; these are forbidden in inversion breaking platforms such as hcp-Fe/Ir(111).

Finally, Fig. 4d summarizes recent progress on material search and magnetic structure studies of noncoplanar magnets with lattice-averaged net spin chirality, especially SkL host compounds<sup>3,13,14,44,45</sup>. As the dimension  $\lambda$  of the magnetic UC increases, magnetic moments cover all directions of the  $S_2$  sphere, and the maximum *gap in angular*

*coverage* (as defined in percent of  $4\pi$ ) approaches zero. For example, noncoplanar antiferromagnets on the left side of Fig. 4d leave large fractions of  $S_2$  out of reach of magnetic moments. Being located at the center of the plot, the C-SkL in the centrosymmetric, breathing kagome magnet  $Gd_3Ru_4Al_{12}$  represents an essential link between long-period, incommensurate magnetic textures, stabilized e.g. by Dzyaloshinskii-Moriya interactions in  $MnSi$ <sup>3,46</sup>, and so-called topological antiferromagnets with canted magnetic moments, such as pyrochlore systems<sup>44</sup>. Although the present C-SkL is locked to the crystal lattice by weak in-plane magnetic anisotropy, confirmed here by ferromagnetic resonance experiments, the magnetic unit cell is large enough so that moments densely cover  $S_2$ , leaving only marginal gaps on the order of 5% of  $4\pi$ .

## Methods

### Cartographic projection

For visualizing the magnetic texture in Fig. 1a, we mapped a magnetic skyrmion onto a sphere in three dimensions, and subsequently mapped from the sphere onto a planar surface using the cartographic Nicolosi globular projection. Let  $(\theta, \varphi)$  denote a point where a line between  $(x, y)$  and the north pole of the sphere penetrates the sphere's surface. These spherical coordinates are identified with  $(x, y)$  in Fig. 1a, upper side, while a point on the sphere is projected back onto the plane using the formalism in ref. 47.

Starting from polar angles  $\theta, \varphi$  on the sphere, the  $x$  and  $y$  coordinates of the planar projection are defined as

$$x = \frac{\pi}{2}R \left( M + \operatorname{sgn}(\varphi - \varphi_0) \sqrt{M^2 + \frac{\cos^2(\theta)}{1 + b^2/d^2}} \right) \quad (3)$$

$$y = \frac{\pi}{2}R \left( N - \operatorname{sgn}(\theta) \sqrt{N^2 - \frac{d^2 \sin^2(\theta)/b^2 + d \sin(\theta) - 1}{1 + d^2/b^2}} \right) \quad (4)$$

with functions

$$M = \frac{b \sin(\theta)/d - b/2}{1 + b^2/d^2}, \quad (5)$$

$$N = \frac{d^2 \sin(\theta)/b^2 + d/2}{1 + d^2/b^2}, \quad (6)$$

$$b = \frac{\pi}{2(\varphi - \varphi_0)} - \frac{2}{\pi}(\varphi - \varphi_0), \quad (7)$$

$$c = \frac{2}{\pi}\theta, \text{ and} \quad (8)$$

$$d = \frac{1 - c^2}{\sin(\theta) - c}. \quad (9)$$

The sphere's radius  $R$  and the reference point for the longitude  $\varphi_0$  can be set to 1 and 0, respectively.

### Sample preparation and characterization

We prepared polycrystals of  $\text{Gd}_3\text{Ru}_4\text{Al}_{12}$  by arc melting of the constituent elements in argon atmosphere, carefully turning pellets at least three times. Subsequently, single crystals were grown from these polycrystals by the floating zone technique under argon flow. Before the melting step, the halogen-lamp based furnace was evacuated to a base pressure of  $8 \cdot 10^{-4}$  Pa, pumping for about three hours. The growth speed in the float zoning step was 2–4 mm/hr. We crushed single crystalline pieces into a fine powder for x-ray diffraction and refined the data by the Rietveld method using the RIETAN software package<sup>48</sup>. In this analysis, we did not find impurity phases with volume fraction larger than 4%. Further, single-crystalline pieces were oriented using a Laue camera, cut with a diamond saw, and hand-polished to a high sheen ( $\sim 1 \mu\text{m}$  grit) for single crystal x-ray diffraction measurements. Using a microscope with Nicolet prism, single-crystalline pieces with small amounts of  $\text{RuAl}_3$  impurity phase, which forms tear-drop shaped inclusions of < 2% volume fraction that are hard to detect by laboratory x-rays, were excluded based on patterns in the surface-reflected light. Finally, magnetization measurements ( $M$ - $H$  curve at  $T = 2$  K,  $M$ - $T$  curve at  $\mu_0 H = 0.1$  T) were used to confirm a systematic evolution of long-range magnetic order in these single crystals.

### Ferromagnetic resonance measurements

In order to avoid unwanted shape anisotropy effects, we polished the  $\text{Gd}_3\text{Ru}_4\text{Al}_{12}$  samples cut within the  $a$ - $c$  plane into a cylindrical disc form, with ellipticity below 4%. The ratio of diameter to thickness was 12 for the final disc, with a thickness of 120  $\mu\text{m}$ .

High-field ferromagnetic resonance (FMR) measurements were performed at École Polytechnique Fédérale de Lausanne (EPFL, Switzerland) using a home built, high-sensitivity, quasi-optical spectrometer operating in the range of 50–420 GHz. This instrument covers a broad magnetic field regime up to 16 T, using a superconducting magnet. Its variable temperature insert operates across the temperature range 1.5–300 K, using the dynamic flow of helium gas, or liquid helium, through a heat exchanger right below the sample space. For more details, see ref. 49.

The overall temperature accuracy of the system is 0.1 K. The polished disc-like sample is mounted on a goniometer with the  $a$ - $c$  plane coinciding with plane of rotation for the static magnetic field, the angular position of which is controllable and detectable via a potentiometer. Rotation proceeded in 5–10 degree steps, at sample temperature  $T = 2$  K. The signal-to-noise ratio of the spectra is improved by recording the field-derivative of the absorbed power  $dP/dH$  using a lock-in technique with magnetic field modulation. The angular-dependent resonance data can be evaluated using the Smit-Beliers-Suhl formula as described in ref. 50. Using the saturation magnetization  $M_S = 7 \mu_B / \text{Gd}^{3+}$ , our fit yields the easy-plane anisotropy constant  $K_1 = -1.944 \cdot 10^6 \text{ erg/cm}^3$  ( $-0.13 \text{ meV} / \text{Gd}^{3+}$ ) and the temperature independent, isotropic  $g$ -factor 2.005.

### Resonant x-ray scattering experiments (Gd- $L_{2,3}$ )

Resonant elastic x-ray scattering (REXS) experiments are carried out in reflection geometry at RIKEN beamline BL19LXU of SPring-8 and beamline BL-3A of Photon Factory, KEK, with the sample mounted inside a cryomagnet. The preparation of Sample A, used to obtain the data in Fig. 3b, is discussed in ref. 11. Sample B, which was used to obtain all other data in this manuscript, has a surface perpendicular to the [110] axis, and was polished to reduce loss of intensity by diffuse scattering of x-rays. The energy of incident x-rays is matched to the  $L_2$  or  $L_3$  absorption edge of Gadolinium, where magnetic scattering involves virtual excitations from the  $2p$  to the  $5d$  atomic shells (Supplementary Fig. 2). The  $5d$  shell is coupled to the dominant magnetic species, the half-filled  $4f$  orbitals, by intra-atomic exchange correlations.

For data in Figs. 1 and 4, which are collected at the Gd- $L_3$  edge ( $E_{x\text{-ray}} = 7.243 \text{ keV}$ ) at BL19LXU of SPring-8, we do not carry out polarization analysis of the diffracted beam. For data in Fig. 3 and Supplementary Fig. 3, which were collected at the Gd- $L_2$  edge ( $E_{x\text{-ray}} = 7.932 \text{ keV}$ ) at BL-3A of Photon Factory,  $\pi - \sigma'$  and  $\pi - \pi'$  components of the diffracted beam are separated using an analyser plate made from pyrolytic graphite (PG-006).

The details of the polarization analysis in the latter case are as follows. Let  $\mathbf{k}_i$  ( $\mathbf{k}_f$ ) be the wavevector of the incoming (outgoing) x-ray beam with polarization vector  $\varepsilon_i$  ( $\varepsilon_f$ ), where the scattering plane is spanned by the two wavevectors; c.f. purple plane in Fig. 1c. Let  $z$  be the direction perpendicular to the scattering plane. The incident beam is  $\pi$ -polarized, so that  $\varepsilon_i \perp \mathbf{e}_z, \mathbf{k}_i$ . In the resonant elastic scattering process, the scattering cross-section  $f_{\text{res}}$  contains a term  $\propto (\varepsilon_i \times \varepsilon_f) \cdot \mathbf{m}(\mathbf{q})$ , where  $\mathbf{q} = \mathbf{k}_f - \mathbf{k}_i$ , and  $\mathbf{m}(\mathbf{q})$  are the momentum transfer and the periodically modulated magnetic moment, respectively (Fig. 1c). In the present case, where  $\varepsilon_i \propto \mathbf{k}_i \times \mathbf{e}_z$  and the scattering plane is aligned with the crystal's hexagonal  $ab$  plane, we separate scattered x-rays with  $\varepsilon_f \parallel \mathbf{e}_z \parallel \mathbf{c}^*$  (i.e.,  $\pi - \sigma'$ ) and  $\varepsilon_f \propto \mathbf{k}_f \times \mathbf{e}_z$  (i.e.,  $\pi - \pi'$ ). Hence  $f_{\text{res}}^{\pi - \sigma'} \propto \mathbf{k}_i \cdot \mathbf{m}(\mathbf{q})$  and  $f_{\text{res}}^{\pi - \pi'} \propto (\mathbf{k}_i \times \mathbf{k}_f) \cdot \mathbf{m}(\mathbf{q}) \propto m_z(\mathbf{q}) \sin(2\theta)$ , where  $2\theta$  is the scattering angle between  $\mathbf{k}_i$  and  $\mathbf{k}_f$ . The observed scattered intensities are  $I \propto |f_{\text{res}}|^2$ .

We obtain integrated intensities  $I_{\pi - \sigma'}$  and  $I_{\pi - \pi'}$  from Gaussian fits to line-cuts in momentum space. As described, the intensity ratio  $R = I_{\pi - \sigma'} / I_{\pi - \pi'}$  at a given magnetic reflection is sensitive to the cycloidal (proper screw) character of the magnetic order by virtue of being large (small) when  $\mathbf{k}_i \cdot (\mathbf{q} - \mathbf{G}')$  is large (small). For proper screw order, magnetic moments arrange themselves perpendicular to the propagation direction ( $\mathbf{q} - \mathbf{G}'$ ), with a finite projection onto both  $\mathbf{e}_z$  (i.e.,  $m_z$ ) and the in-plane vector  $\mathbf{e}_\perp = (\mathbf{q} - \mathbf{G}') \times \mathbf{e}_z$  (i.e.,  $\mathbf{m}_{ip}$ ). Here we introduce  $\mathbf{G}'$ , the closest reciprocal lattice vector to  $\mathbf{q}$ , and  $\mathbf{e}_z$  a unit vector along the  $c$ -direction. It follows  $R \sin^2(2\theta) \propto [\mathbf{k}_i \cdot \mathbf{e}_\perp(\mathbf{q})]^2$  for a proper screw-type order, as demonstrated for  $\text{Gd}_3\text{Ru}_4\text{Al}_{12}$  in Fig. 3b, c. Moreover,  $R$  provides information on the degree of elliptical distortion, capturing e.g. the ratio  $(m_y/m_z)^2$  for a proper screw propagating along  $\mathbf{e}_x$ , written as  $\mathbf{e}_y \cdot m_y \sin(2\pi x/\lambda) + \mathbf{e}_z \cdot m_z \cos(2\pi x/\lambda)$ , where  $\mathbf{e}_x, \mathbf{e}_y, \mathbf{e}_z$  are Cartesian unit vectors aligned so that  $\mathbf{e}_x \parallel \mathbf{q}$ . In real materials with large (classical) magnetic moments, where the length of the moment is fixed to be spatially uniform in space, this type of deformed screw can be realized by anharmonic distortion of the proper screw texture, as shown in Fig. 3b (inset).

## Data availability

The data supporting the findings of this study are available from the corresponding author upon reasonable request.

Received: 17 September 2023; Accepted: 26 April 2024;

Published online: 23 May 2024

## References

- Bogdanov, A. & Yablonsky, D. Thermodynamically stable vortexes in magnetically ordered crystals: mixed state of magnetics. *J. Exp. Theor. Phys.* **95**, 178 (1989).
- Mühlbauer, S. et al. Skyrmion Lattice in a Chiral Magnet. *Science* **323**, 915 (2009).
- Tokura, Y. & Kanazawa, N. Magnetic Skyrmion Materials. *Chem. Rev.* **5**, 2857 (2021).
- Binz, B., Vishwanath, A. & Aji, V. Theory of the Helical Spin Crystal: A Candidate for the Partially Ordered State of MnSi. *Phys. Rev. Lett.* **96**, 207202 (2006).
- Binz, B. & Vishwanath, A. Theory of helical spin crystals: Phases, textures, and properties. *Phys. Rev. B* **74**, 214408 (2006).
- Okubo, T., Chung, S. & Kawamura, H. Multiple-q States and the Skyrmion Lattice of the Triangular-Lattice Heisenberg Antiferromagnet under Magnetic Fields. *Phys. Rev. Lett.* **108**, 017206 (2012).
- Hayami, S., Lin, S.-Z. & Batista, C. Bubble and skyrmion crystals in frustrated magnets with easy-axis anisotropy. *Phys. Rev. B* **93**, 184413 (2016).
- Ozawa, R., Hayami, S. & Motome, Y. Zero-Field Skyrmions with a High Topological Number in Itinerant Magnets. *Phys. Rev. Lett.* **118**, 147205 (2017).
- Hayami, S., Ozawa, R. & Motome, Y. Effective bilinear-biquadratic model for noncoplanar ordering in itinerant magnets. *Phys. Rev. B* **95**, 224424 (2017).
- Wang, Z., Su, Y., Lin, S.-Z. & Batista, C. Skyrmion Crystal from RKKY Interaction Mediated by 2D Electron Gas. *Phys. Rev. Lett.* **124**, 207201 (2020).
- Hirschberger, M. et al. Skyrmion phase and competing magnetic orders on a breathing kagomé lattice. *Nat. Commun.* **10**, 5831 (2019).
- Khanh, N. et al. Nanometric square skyrmion lattice in a centrosymmetric tetragonal magnet. *Nat. Nanotechnol.* **15**, 444 (2020).
- Matsumura, T. et al. Distorted triangular skyrmion lattice in a noncentrosymmetric tetragonal magnet, Preprint at <https://arxiv.org/abs/2306.14767> (2023).
- Singh, D. et al. Transition between distinct hybrid skyrmion textures through their hexagonal-to-square crystal transformation in a polar magnet. *Nat. Commun.* **14**, 8050 (2023).
- Binz, B. & Vishwanath, A. Chirality induced anomalous-Hall effect in helical spin crystals. *Phys. B: Condens. Matter.* **403**, 1336 (2008).
- Heinze, S. et al. Spontaneous atomic-scale magnetic skyrmion lattice in two dimensions. *Nat. Phys.* **7**, 713 (2011).
- Nagaosa, N. Emergent inductor by spiral magnets. *Jpn. J. Appl. Phys.* **58**, 120909 (2019).
- Sorn, S., Yang, L. & Paramekanti, A. Resonant optical topological Hall conductivity from skyrmions. *Phys. Rev. B* **104**, 134419 (2021).
- Kato, Y., Okamura, Y., Hirschberger, M., Tokura, Y. & Takahashi, Y. Topological magneto-optical effect from skyrmion lattice. *Nat. Commun.* **14**, 5416 (2023).
- Hirschberger, M. et al. Topological Nernst effect of the two-dimensional skyrmion lattice. *Phys. Rev. Lett.* **125**, 076602 (2020).
- Takagi, R. et al. Square and rhombic lattices of magnetic skyrmions in a centrosymmetric binary compound. *Nat. Commun.* **13**, 1472 (2022).
- Zhang, H., Wang, Z., Dahlbom, D., Baros, K. & Batista, C. D. CP<sup>2</sup> skyrmions and skyrmion crystals in realistic quantum magnets. *Nat. Commun.* **14**, 3626 (2023).
- Hayami, S. & Yambe, R. Locking of skyrmion cores on a centrosymmetric discrete lattice: Onsite versus offsite. *Phys. Rev. Res.* **3**, 043158 (2021).
- v. Bergmann, K., Menzel, M., Kubetzka, A. & Wiesendanger, R. Influence of the Local Atom Configuration on a Hexagonal Skyrmion Lattice. *Nano Lett.* **15**, 3280 (2015).
- Wiesendanger, R. Nanoscale magnetic skyrmions in metallic films and multilayers: a new twist for spintronics. *Nat. Rev. Mater.* **1**, 16044 (2016).
- Gutzeit, M., Drevelow, T., Goerzen, M. A., Haldar, S. & Heinze, S. Spontaneous square versus hexagonal nanoscale skyrmion lattices in Fe/Ir(111). *Phys. Rev. B* **108**, L060405 (2023).
- Hirschberger, M. et al. Lattice-commensurate skyrmion texture in a centrosymmetric breathing kagome magnet, Supplementary Material at <https://doi.org/10.1038/s41535-024-00654-2>.
- Hirschberger, M., Hayami, S. & Tokura, Y. Nanometric skyrmion lattice from anisotropic exchange interactions in a centrosymmetric host. *New J. Phys.* **23**, 023039 (2021).
- Koehler, W. Magnetic Structures of Rare Earth Metals and Alloys, edited by Elliott, R., Springer New York (1972).
- Jensen, J. & Mackintosh, A. R. Rare Earth Magnetism: Structures and Excitations, Clarendon Press (1991).
- Venturini, G., Fruchart, D. & Malaman, B. Incommensurate magnetic structures of RMn<sub>6</sub>Sn<sub>6</sub> (R = Sc, Y, Lu) compounds from neutron diffraction study. *J. Alloys Compd.* **236**, 102 (1996).
- Zheludev, A. et al. Field-Induced Commensurate-Incommensurate Phase Transition in a Dzyaloshinskii-Moriya Spiral Antiferromagnet. *Phys. Rev. Lett.* **78**, 4857 (1997).
- Simeth, W. et al. Resonant Elastic X-Ray Scattering of Antiferromagnetic Superstructures in EuPtSi<sub>3</sub>. *Phys. Rev. Lett.* **130**, 266701 (2023).
- Matsumura, T. et al. Chiral Soliton Lattice Formation in Monoaxial Helimagnet Yb(Ni<sub>1-x</sub>Cu<sub>x</sub>)<sub>3</sub>Al<sub>9</sub>. *J. Phys. Soc. Jpn.* **86**, 124702 (2017).
- Okumura, S., Kato, Y. & Motome, Y. Lock-in of a Chiral Soliton Lattice by Itinerant Electrons. *J. Phys. Soc. Jpn.* **87**, 033708 (2018).
- Wilson, J., Salvo, F. D. & Mahajan, S. Charge-density waves and superlattices in the metallic layered transition metal dichalcogenides. *Adv. Phys.* **24**, 117 (1975).
- Fleming, B. M., Moncton, D. E., McWhan, D. B. & DiSalvo, F. J. Broken Hexagonal Symmetry in the Incommensurate Charge-Density Wave Structure of 2H-TaSe<sub>2</sub>. *Phys. Rev. Lett.* **45**, 576 (1980).
- Bak, P. Commensurate phases, incommensurate phases and the devil's staircase. *Rep. Prog. Phys.* **45**, 587 (1982).
- Hase, M., Terasaki, I. & Uchinokura, K. Observation of the spin-Peierls transition in linear Cu<sup>+</sup> (spin-1/2) chains in an inorganic compound CuGeO<sub>3</sub>. *Phys. Rev. Lett.* **70**, 3651 (1993).
- Kiryukhin, V., Keimer, B. & Moncton, D. E. Direct Observation of a Magnetic Field Induced Commensurate-Incommensurate Transition in a Spin-Peierls System. *Phys. Rev. Lett.* **74**, 1669 (1995).
- Kiryukhin, V. & Keimer, B. Incommensurate lattice modulation in the spin-Peierls system CuGeO<sub>3</sub>. *Phys. Rev. B* **52**, R704(R) (1995).
- Kiryukhin, V., Keimer, B., Hill, J. & Vigliante, A. Soliton Lattice in Pure and Diluted CuGeO<sub>3</sub>. *Phys. Rev. Lett.* **76**, 4608 (1996).
- Leonov, A. O. & Mostovoy, M. Multiply periodic states and isolated skyrmions in an anisotropic frustrated magnet. *Nat. Commun.* **6**, 8275 (2015).
- Gardner, J., Gingras, M. & Greedan, J. Magnetic pyrochlore oxides. *Rev. Mod. Phys.* **82**, 53 (2010).
- Takagi, H. et al. Spontaneous topological Hall effect induced by non-coplanar antiferromagnetic order in intercalated van der Waals materials. *Nat. Phys.* **19**, 961–968 (2023).
- Bak, P. & Jensen, M. Theory of helical magnetic structures and phase transitions in MnSi and FeGe. *J. Phys. C: Solid State Phys.* **13**, L881 (1980).
- Snyder, J. P. An Album of Map Projections. *U.S. Geological Survey* **1453**, 234 (1989).

48. Izumi, F. & Momma, K. Three-Dimensional Visualization in Powder Diffraction. *Solid State Phenom.* **130**, 15 (2007).
49. Náfrádi, B., Gaál, R., Sienkiewicz, A., Fehér, T. & Forró, L. Continuous-wave far-infrared ESR spectrometer for high-pressure measurements. *J. Magn. Reson.* **195**, 206 (2008).
50. Ehlers, D. et al. Exchange anisotropy in the skyrmion host GaV<sub>4</sub>S<sub>8</sub>. *J. Phys. Condens. Matter* **29**, 065803 (2017).
51. Butykai, Á. et al. Squeezing the periodicity of Néel-type magnetic modulations by enhanced Dzyaloshinskii-Moriya interaction of 4d electrons. *npj Quantum Mater.* **7**, 26 (2022).

## Acknowledgements

We thank Taro Nakajima for support regarding resonant elastic x-ray scattering (REXS) experiments at beamline BL-3A of Photon Factory. Akiko Kikkawa provided guidance regarding single crystal synthesis. We acknowledge Ferenc Simon for fruitful discussions and technical support at EPFL, and Dieter Ehlers for providing his software to model the ferromagnetic resonance data. We are also grateful to Vladimir Tsurkan for polishing the samples for FMR. REXS measurements at the Institute of Material Structure Science of the High Energy Accelerator Research Organization (KEK) and at SPring-8 BL19LXU were carried out under the approval of the Photon Factory program advisory committee (Proposal No. 2020G665) and under grant number 20210007, respectively. M.He. and H.-A. K.v.N. acknowledge funding within the joint RFBR-DFG research project contract No. 19-51-45001 and KR2254/3-1. S.E. and Ma.Hi. benefited from JSPS KAKENHI Grant No. 22H04463 and 23H05431, while also acknowledging grants by the Murata Science Foundation, the Yamada Science Foundation, the Hattori Hokokai Foundation, the Iketani Science and Technology Foundation, the Mazda Foundation, the Casio Science Promotion Foundation, the Inamori Foundation, the Kenjiro Takayanagi Foundation, and the Marubun foundation through their Exchange Grant. This work is partially funded by the Deutsche Forschungsgemeinschaft (DFG, German Research Foundation) under project numbers 518238332 and TRR 360–492547816 and by the Japan Science and Technology Agency via Core Research for Evolutional Science and Technology (CREST) Grant Nos. JPMJCR1874, JPMJCR20T1 (Japan), and by FOREST No. JPMJFR2238.

## Author contributions

Ma.Hi., I.K., Y.To. and T.-h.A. conceived the project. Ma.Hi. synthesized and characterized the single crystals. M.He., B.G.S., H.-A.K.v.N. and L.F. carried

out electron spin-resonance experiments at EPFL. Ma.Hi., L.S., H.O. and Y.Ta. performed REXS at SPring-8. Ma.Hi., L.S., S.G., K.K., H.S., H.N. and Y.Y. carried out REXS measurements at BL-3A of Photon Factory (KEK). Ma.Hi. and S.E. were in charge of spin model calculations. Ma.Hi. wrote the manuscript in close collaboration with M.M.H. and S.E., and with contributions and comments from all co-authors.

## Competing interests

The authors declare no competing interests.

## Additional information

**Supplementary information** The online version contains supplementary material available at <https://doi.org/10.1038/s41535-024-00654-2>.

**Correspondence** and requests for materials should be addressed to Max Hirschberger.

**Reprints and permissions information** is available at <http://www.nature.com/reprints>

**Publisher's note** Springer Nature remains neutral with regard to jurisdictional claims in published maps and institutional affiliations.

**Open Access** This article is licensed under a Creative Commons Attribution 4.0 International License, which permits use, sharing, adaptation, distribution and reproduction in any medium or format, as long as you give appropriate credit to the original author(s) and the source, provide a link to the Creative Commons licence, and indicate if changes were made. The images or other third party material in this article are included in the article's Creative Commons licence, unless indicated otherwise in a credit line to the material. If material is not included in the article's Creative Commons licence and your intended use is not permitted by statutory regulation or exceeds the permitted use, you will need to obtain permission directly from the copyright holder. To view a copy of this licence, visit <http://creativecommons.org/licenses/by/4.0/>.

© The Author(s) 2024